Rapid Coarsening of Ion Beam Ripple Patterns by Defect Annihilation

Henri Hansen,[1] Alex Redinger,[1,2] Sebastian Messlinger,[1] Georgiana Stoian,[1,*] Joachim Krug,[3] and Thomas Michely[2,†]

[1]*I. Physikalisches Institut, RWTH Aachen, 52056 Aachen, Germany*

[2]*II. Physikalisches Institut, Universität zu Köln, 50937 Köln, Zülpicher Straße 77, Germany*

[3]*Institut für Theoretische Physik, Universität zu Köln, 50937 Köln, Zülpicher Straße 77, Germany*

(Received 30 October 2008; published 7 April 2009)

Ripple patterns formed on Pt(111) through grazing incidence ion beam erosion coarsen rapidly. At and below 450 K coarsening of the patterns is athermal and kinetic, unrelated to diffusion and surface free energy. Similar to the situation for sand dunes, coarsening takes place through annihilation reactions of mobile defects in the pattern. The defect velocity derived on the basis of a simple model agrees quantitatively with the velocity of monatomic steps illuminated by the ion beam.

DOI: 10.1103/PhysRevLett.102.146103 PACS numbers: 68.35.Ct, 61.80.Jh, 61.82.Bg, 68.37.Ef

Coarsening, i.e., the increase of the characteristic feature size with time, is a well known and ubiquitous phenomenon in the physics of structure formation. Ostwald ripening [1], grain growth [2], or grain boundary grooving [3] are examples for coarsening phenomena driven by the minimization of surface or interface energy in a system. Coarsening also takes place in systems far from equilibrium with nonconserved particle numbers, e.g., in molecular beam epitaxy (MBE) or ion beam erosion.

Siegert [4] and Moldovan and Golubović [5] first realized that coarsening in MBE and ion beam erosion under conditions where kinetically preferred facets are established is enabled by defects in the evolving pattern. The demand for reduction of effective system energy stored in the facet edges drives the reduction of edge length and gives rise to the motion of defects and their subsequent annihilation reactions. The facet edge mobility itself requires thermally activated surface diffusion and is thus dependent on the characteristic feature size λ of the pattern and on temperature T. The feature size is found to develop with time t according to a power law $\lambda \propto t^n$ with coarsening exponents n ranging from $1/3$ to $1/4$ depending on the symmetry of the crystalline substrate [5,6], in partial accordance with experiments [7–9].

However, there are also situations where coarsening is not an energy minimizing process. Using scanning tunneling microscopy (STM), here we show that under grazing incidence ion erosion of a crystalline surface rapid, athermal coarsening of the ripple pattern takes place through the annihilation of mobile defects, which are driven by the ion beam along the ripple direction. The mechanism is similar to that described by Werner and Kocurek [10] for coarsening in transverse aeolian sand dunes, where defects are driven by the wind *perpendicular* to the crest lines. This establishes a connection between coarsening of ion beam ripples ($\lambda \approx 10^{-8}$ m) and dunes ($\lambda \approx 10^{3}$ m), complementing existing theoretical attempts to use models of aeolian ripple formation for the description of ion beam ripples [11,12].

Ripple patterns form under ion erosion of solid surfaces through a variety of different mechanisms [13], and in all cases such patterns contain a certain density of defects that reflect the random fluctuations during the initial stages of the evolution. Defect density has been used as a measure for the degree of order in ion-induced ripple patterns [14,15], but the dynamical evolution of defects and their relation to coarsening behavior has so far been studied only on a qualitative level [16,17]. In the specific case of grazing incidence erosion of crystalline surfaces considered here, the topography evolution can be largely reduced to the ion-induced propagation of surface steps [18,19]. This basic simplicity of the dynamics allows us to *quantitatively* relate the coarsening behavior to the fundamental time constant of the process, the propagation velocity of individual steps. We expect that the present work may direct attention to the relation of defect concentrations and coarsening rates also for other scenarios of ion-induced ripple formation.

The experiments were performed in an ultrahigh vacuum variable temperature STM apparatus with a base pressure of 10^{-11} mbar. Cleaning of the Pt(111) sample was accomplished by cycles of sputtering and flash annealing to 1273 K. For the coarsening experiments the clean surface was exposed to ion fluences F between 1 and 300 monolayer equivalent (MLE) of 5 keV Ar^+ ions with a flux of 4.6×10^{-3} MLE/s incident along the $[\bar{1}\,\bar{1}\,2]$ direction at an angle of $\vartheta = 83°$ to the surface normal and at temperatures from 350 to 550 K. For simplicity the quantity monolayer equivalent is used, where 1 MLE $= 1.504 \times 10^{19}$ ions/m^2 corresponds to the Pt(111) surface atomic density. STM imaging was performed at room temperature, where the resulting patterns are frozen.

Coarsening during 5 keV Ar^+ grazing incidence ion exposure of Pt(111) is visualized in Figs. 1(a)–1(f) after fluences from 1 MLE up to 300 MLE. As is visible in Fig. 1(a) after exposure to 1 MLE, the formation of a ripple pattern is rapid. The pattern is aligned along the projection of the ion beam direction on the surface. In the initial stage

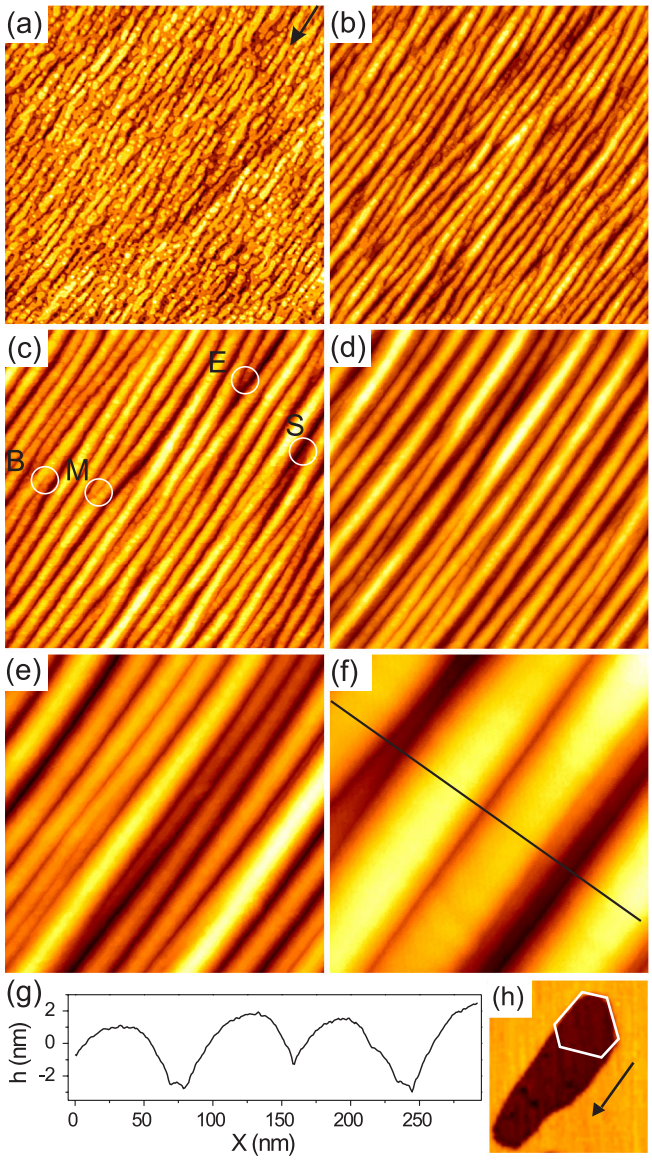

FIG. 1 (color online). (a)–(f) STM topographs of Pt(111) after exposure to 5 keV Ar^+ incident at an angle $\vartheta = 83°$ at 450 K. The scan size is always 2450 Å × 2450 Å. The ion fluences are (a) 1 MLE, (b) 5 MLE, (c) 20 MLE, (d) 70 MLE, (e) 160 MLE, and (f) 300 MLE. The projection of the ion beam direction onto the surface is indicated by an arrow in (a). The four types of defects in the ripple pattern are circled in (c). They are start (S), end (E), bifurcation (B), and merger (M) defects. (g) Displays a height profile along the coordinate X of the line indicated in (f). (h) A hexagonal vacancy island formed after sputtering and equilibration at 750 K [23] (indicated by the white hexagon) is elongated through the motion of the illuminated steps in beam direction during grazing incidence ion exposure at 550 K.

steps of monatomic height can still be distinguished in the STM topograph. The mechanisms of pattern formation have been described in a previous publication [18]. Briefly, grazing incidence ions cause only little sputtering. Nevertheless, after an induction time the excess surface vacancies aggregate to vacancy clusters which expose an illuminated step to the ion beam. The sputtering yield for an illuminated step edge is 7.7 ± 0.9, a factor of 100 higher than the sputtering yield of ions impinging on the terrace [19]. Thus illuminated steps are rapidly driven forward in the direction of the ion beam with a normalized velocity $v = 28 \pm 3$ nm/MLE for 5 keV Ar^+, resulting in long vacancy grooves [Fig. 1(h)]. Ordering of the vacancy grooves in the direction normal to the ripple ridges is caused by vacancy depletion in the terraces between the grooves and the adatom repulsion effect [18]. The initial pattern with monolayer corrugation amplitude [Fig. 1(a)] transforms into a three-dimensional ripple pattern through preferential nucleation of vacancies in grooves: the step edge barrier for vacancies prevents their annealing at ascending steps, thereby suppressing material transport between different layers [20,21].

As is visible in Figs. 1(b)–1(f), λ strongly increases with F. Figure 2 represents the dependence of λ on F quantitatively. After a rapid initial increase of λ up to 20 MLE it becomes a linear function of F. Within the limits of error the wavelength increase is identical for 350 and 450 K evidencing the athermal nature of the coarsening. Above 450 K step edge diffusion sets in, causing a significant increase of the initial wavelength [18]. Besides an apparent upward shift, the functional dependence of λ on F in the thermal regime at 550 K is still similar to the lower temperature cases.

The inset of Fig. 2 displays the evolution of the surface roughness σ with F. A power law behavior with $\sigma \propto F^{\beta}$ is found over a fluence range of more than two decades. The exponents β are 0.50, 0.48, and 0.59 for 350, 450, and 550 K, respectively. An exponent $\beta = 1/2$ results for a Poisson model, i.e., for a situation where material transport between different atomic layers is suppressed (large step edge barrier for surface vacancies) [22]. The observed preferential nucleation of surface vacancies at the bottom of grooves is consistent with this scenario.

The formation of stable kinetically preferred facets in the pattern (slope selection) would require the identity of

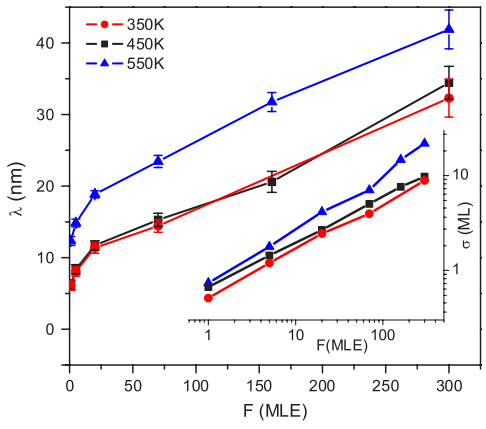

FIG. 2 (color online). Pattern wavelength λ and roughness σ (inset) as a function of ion fluence F for 350 K (full dots), 450 K (full squares), and 550 K (full up triangles). Lines are to guide the eye.

the exponents n and β, which is not observed here. Indeed, the height profile of Fig. 1(g) taken through the ripples of Fig. 1(f) does not display a single set of preferred facets but rather a parabolic ridge profile.

It is well visible in Fig. 1 that defects originating from the initial randomness of nucleation and coalescence of monolayer vacancy islands are present in all stages of pattern evolution. Four types of topological pattern defects are circled and labeled in Fig. 1(c). With respect to the ion beam direction we distinguish the start (S), end (E), bifurcation (B), and merger (M) of ridges. For clarity, the four defects are sketched schematically in Fig. 3(a). Although the identification of these defects appears to be straightforward, the distinction between S and B defects requires a quantitative criterion to decide whether an emerging ridge (viewed in the downstream direction) branches off an existing ridge or starts anew in the valley between two ridges. The criterion used in this work is sketched in the inset of Fig. 3(a). If slightly downstream to the defect the height $\Delta r \leq \Delta h/2$ [as for a profile between the white arrows near B in Fig. 3(a)], we consider it as a B defect, and if $\Delta r \geq \Delta h/2$ as an S defect [as for a profile between the white arrows near S in Fig. 3(a)]. Similar considerations apply to E and M defects. As λ is uniform over the sample for any topograph of lateral dimension much larger than λ, we obtain for the numbers of specific defects $N_S + N_B \approx N_E + N_M$; i.e., the number of ridges entering a topograph is approximately equal to that leaving it.

As a key to the understanding of coarsening through defect motion, we consider now a simple start S defect. It consists of an array of illuminated monatomic steps which consequently will move in the beam direction with a speed similar to that of a single step. To the contrary, an end E defect consists of an array of steps not illuminated by the ion beam and is thus immobile. If the ridge originating from an S defect terminates in an E defect, the ion beam will move the S defect towards the E defect until they annihilate. As a consequence, a ridge is removed and thus the average wavelength has increased.

We derive a simple analytical formula relating the defect concentration to coarsening (compare also [5,10]) for the simplified defect pattern containing only S and E defects in Fig. 3(b). The field of area $A = X \times Y$ has a total ridge length L with an average separation λ such that $A = \lambda L$. The total number of defects in the field of area A is N, the defect density ρ correspondingly $\rho = N/A$. The S defects form a fraction γ ($\gamma = 1/2$ if we consider only S and E defects) of all defects and move with a velocity v. Therefore the total ridge length decreases with ion fluence according to

$$\frac{dL}{dF} = -v\gamma N. \tag{1}$$

In order to obtain the change of λ with fluence we rearrange the identity $dA/dF = 0 = L(d\lambda/dF) + \lambda(dL/dF)$ to obtain

$$\frac{d\lambda}{dF} = -\frac{\lambda}{L}\frac{dL}{dF} = \frac{\lambda}{L} v\gamma N = \lambda^2 v\gamma\rho. \tag{2}$$

As we are able to measure λ and ρ as a function of F from our STM topographs, Eq. (2) allows us to obtain a quantitative value for v.

Assuming the fraction of mobile S defects to be $\gamma = \frac{1}{4}$ of all defects and the mobility of E, B, and M defects to be negligible yields the velocities v represented in Fig. 4. The total defect density ρ as a function of ion fluence is plotted in the inset of Fig. 4. The evaluation of ρ was feasible for ion fluences of 5 MLE and larger. It decreases from 5 to 300 MLE by more than a factor of 25. For 350, 450, and 550 K the average v is 16 ± 2, 16 ± 1, and 8 ± 1 nm/MLE, respectively. For the athermal regime v resulting from our crude analysis agrees to better than a factor of 2 with the velocity $v = 28$ nm/MLE of a single step driven by the ion beam. We consider this agreement as strong evidence for coarsening driven by defect motion, which itself results from step motion in the beam direction

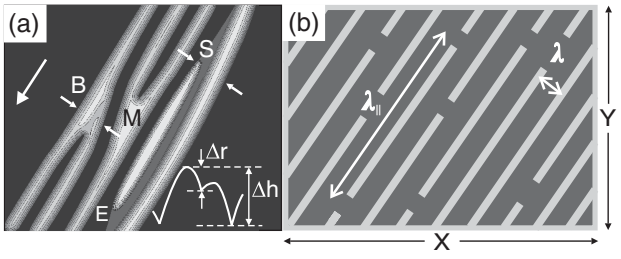

FIG. 3. (a) Schematic representation of the start (S), end (E), bifurcation (B), and merger (M) defects pointed out in Fig. 1(c). Inset: Sketch for the quantitative distinction between S and B defects (see text). (b) Schematic sketch of a ripple pattern with S and E defects only (see text). The large arrow in (a) indicates the beam direction.

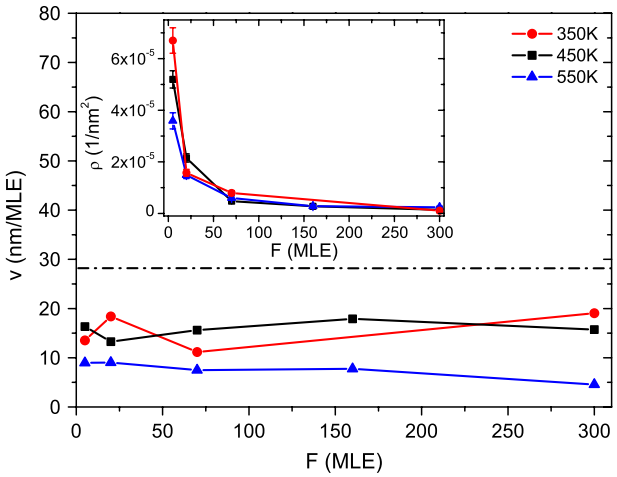

FIG. 4 (color online). Defect velocity v and defect density ρ as a function of fluence F (inset) at 350 K (full dots), 450 K (full squares), and 550 K (full up triangles). The dash-dotted line corresponds to the velocity of a single monatomic step hit by ions at right angles. Lines are to guide the eye.

due to selective step erosion. Note that our analysis did not use any free parameter. Although the data scatter around the respective average value, there is no trend for a decrease of v with increasing λ for 350 and 450 K. This is in contrast to continuum models for defect-driven coarsening of ripple patterns such as the model of Golubović and Levandovsky [6] for fcc(110) surfaces, which predicts that $v \propto 1/\lambda^{3/2}$. The fact that the defect velocity is a constant in our system supplies further evidence for a distinct type of coarsening. In the thermal regime at 550 K coarsening is apparently influenced by diffusion giving rise to the smaller v and the tendency for a decrease in v with F.

A characteristic feature of models for defect-mediated coarsening is the existence of multiple length scales which increase at different rates [4–6]. In the present case a second relevant scale is the mean spacing $\lambda_\parallel$ between defects along the direction of the ridges [compare Fig. 3(b)], which is related to the pattern wavelength λ and the defect density ρ through $\rho = 1/(\lambda\lambda_\parallel)$. Computing $\lambda_\parallel$ from the data for λ and ρ we find that $\lambda_\parallel \gg \lambda$ at all times, and for $F \geq 20$ MLE $\lambda_\parallel$ generally exceeds the topograph size, as is also evident from Figs. 1(c)–1(f). Inserting $\rho = 1/(\lambda\lambda_\parallel)$ on the right-hand side of (2) shows that it is the ridge aspect ratio $\lambda_\parallel/\lambda \gg 1$ which gives rise to the large factor relating the step velocity v to the coarsening rate $d\lambda/dF$.

The model presented above is oversimplified in several respects. A unique velocity v in the beam direction and a fraction $\gamma = 1/4$ have been assumed here mainly for lack of an adequate description for the velocities of all defects. As described above, S and B defects differ for a large number of situations only gradually. While the extreme case of an S defect with $\Delta r \approx \Delta h$ will have a velocity not significantly different from that of a single step, the velocity of a B defect with $\Delta r \approx 0$ will vanish. The cases in between may have intermediate velocities. As S and B defects make up $1/2$ of all defects, it appears still reasonable to assume $\gamma = 1/4$ with a uniform v. The neglected M defects also expose steps to the ion beam and thus must be assumed to move, create ridge length, and thus reduce the coarsening rate. However, we rarely observe M defects in their pure form, as they tend to transform into immobile E defects when the groove cuts sideways through one of the branching ridges [see Fig. 3(a)]. Finally, even a perfect S defect is likely to move more slowly than a single illuminated step edge. Channeling ions (a significant fraction of all ions) entering the crystal at an isolated monatomic step travel just one layer underneath the surface and are likely to cause significant sputtering when dechanneling. In contrast, channeling ions entering the crystal close to the bottom of an S defect deposit their energy well below the surface of the ridge, cause little sputtering, and therefore give rise to a comparatively lower step velocity, as observed.

In conclusion, for grazing incidence ion erosion there is a regime of athermal coarsening in the ensuing ripple pattern resulting from mobile defects with a velocity related to the velocity of a single monatomic step exposed to the ion beam. To obtain additional information on the mobility of complex defect structures, experimental investigations applying *in situ* imaging of the developing pattern appear to be most suitable.

We acknowledge financial support through DFG and help from Oliver Ricken.

*Present address: Solid State Physics, University of Twente, P.O. Box 217, 7500 AE Enschede, The Netherlands.
†michely@ph2.uni-koeln.de

[1] W. Ostwald, Z. Phys. Chem. **34**, 495 (1900).
[2] J. Stavans, Rep. Prog. Phys. **56**, 733 (1993).
[3] W. W. Mullins, J. Appl. Phys. **28**, 333 (1957).
[4] M. Siegert, Phys. Rev. Lett. **81**, 5481 (1998).
[5] D. Moldovan and L. Golubović, Phys. Rev. E **61**, 6190 (2000).
[6] L. Golubović and A. Levandovsky, Phys. Rev. E **77**, 051606 (2008).
[7] J. K. Zuo and J. F. Wendelken, Phys. Rev. Lett. **78**, 2791 (1997).
[8] S. Rusponi, G. Costantini, C. Boragno, and U. Valbusa, Phys. Rev. Lett. **81**, 2735 (1998).
[9] T. Michely, M. Kalff, G. Comsa, M. Strobel, and K. H. Heinig, Phys. Rev. Lett. **86**, 2589 (2001).
[10] B. T. Werner and G. Kocurek, Geology **27**, 727 (1999).
[11] T. Aste and U. Valbusa, Physica (Amsterdam) **332A**, 548 (2004).
[12] M. Castro, R. Cuerno, L. Vázquez, and R. Gago, Phys. Rev. Lett. **94**, 016102 (2005).
[13] W. L. Chan and E. Chason, J. Appl. Phys. **101**, 121301 (2007).
[14] A. Cuenat, H. B. George, K.-C. Chang, J. M. Blakely, and M. J. Aziz, Adv. Mater. **17**, 2845 (2005).
[15] A. Keller, S. Facsko, and W. Möller, New J. Phys. **10**, 063004 (2008).
[16] S. Habenicht, K. P. Lieb, J. Koch, and A. D. Wieck, Phys. Rev. B **65**, 115327 (2002).
[17] M. Stepanova and S. K. Dew, J. Vac. Sci. Technol. B **24**, 592 (2006).
[18] H. Hansen, A. Redinger, S. Messlinger, G. Stoian, Y. Rosandi, H. M. Urbassek, U. Linke, and T. Michely, Phys. Rev. B **73**, 235414 (2006).
[19] A. Redinger, Y. Rosandi, H. M. Urbassek, and T. Michely, Phys. Rev. B **77**, 195436 (2008).
[20] D. Cherns, Philos. Mag. **36**, 1429 (1977).
[21] B. Poelsema, R. Kunkel, L. K. Verheij, and G. Comsa, Phys. Rev. B **41**, 11 609 (1990).
[22] P. I. Cohen, G. S. Petrich, P. R. Pukite, G. J. Whaley, and A. S. Arrott, Surf. Sci. **216**, 222 (1989).
[23] T. Michely and G. Comsa, Surf. Sci. **256**, 217 (1991).